



Cite this: DOI: 10.1039/c8nr00068a

## High-temperature solvent-free sulfidation of MoO<sub>3</sub> confined in a polypyrrole shell: MoS<sub>2</sub> nanosheets encapsulated in a nitrogen, sulfur dual-doped carbon nanoprism for efficient lithium storage†

Ying Liu,<sup>a</sup> Jixin Zhu,<sup>id</sup> Jingsan Xu,<sup>id</sup> Siliang Liu,<sup>a</sup> Le Li,<sup>a</sup> Chao Zhang<sup>id</sup> \*<sup>a</sup> and Tianxi Liu<sup>id</sup> \*<sup>a</sup>

Hierarchical nanostructured metal sulfides in a rectangular prism shape are highly attractive as a promising electrode material for lithium ion energy storage. Herein, we develop a simultaneous pyrolysis and sulfidation strategy to synthesize yolk-shelled MoS<sub>2</sub>@nitrogen, sulfur dual-doped carbon (MoS<sub>2</sub>@NSC) nanoprisms. Upon encapsulating MoO<sub>3</sub> nanoprisms into a polypyrrole (PPy) shell, a high-temperature solvent-free sulfidation reaction from MoO<sub>3</sub> to hierarchical MoS<sub>2</sub> nanosheets could take place within the PPy nanoreactor, and the PPy nanoreactor simultaneously converted into NSC hollow nanoprisms. Owing to the compositional and structural superiority, the MoS<sub>2</sub>@NSC nanoprisms with a well-defined sheet-in-prism superstructure manifested enhanced electrochemical activity as a promising anode material for lithium-ion batteries including a high reversible capacity (960 mA h g<sup>-1</sup> at 0.1 A g<sup>-1</sup>), excellent cycling stability (800 mA h g<sup>-1</sup> at 0.1 A g<sup>-1</sup> up to 300 cycles), and superior rate capability (440 mA h g<sup>-1</sup> at 2 A g<sup>-1</sup>).

Received 4th January 2018,  
Accepted 21st March 2018

DOI: 10.1039/c8nr00068a  
rsc.li/nanoscale

### 1. Introduction

Rechargeable lithium ion batteries (LIBs) have significantly expanded the application range of energy storage devices in portable electronic devices, hybrid electric vehicles, *etc.*<sup>1–3</sup> Among the various components of LIBs, negative electrodes

inevitably play key roles in determining the overall performance of LIBs, and therefore tremendous interest has been shown to develop low-cost and active materials such as transition-metal compounds as promising next-generation anode materials.<sup>4–8</sup> Two-dimensional (2D) transition-metal dichalcogenides (TMDs) especially molybdenum disulfides (MoS<sub>2</sub>) have attracted much attention in view of their low cost, high theoretical capacity and natural abundance.<sup>9–12</sup> Nevertheless, the applications of MoS<sub>2</sub> are greatly hindered by its intrinsically limited electrical conductivity and poor cycling stability due to the large volume variations during the intercalation and extraction of Li ions. Moreover, the tendency of nano-sized MoS<sub>2</sub> to restack into aggregated large particles further deteriorates its performance.<sup>13–15</sup>

To circumvent these obstacles, engineering hierarchical MoS<sub>2</sub> nanostructures with efficient ion and electron transport is attractive to provide new opportunities to enhance the lithium storage capability in both fundamental and practical applications. Basically, rational design and synthesis of MoS<sub>2</sub> nanosheets into hierarchical structures including spherical, tubular and polyhedral shapes would greatly boost the electrochemical performance due to their multiple intriguing properties as follows: (i) hierarchical MoS<sub>2</sub> nanosheets with a high surface area provide abundant electrochemically active sites and a large contacting area between the electrode and electrolyte<sup>16</sup> and (ii) optimized voids provide buffer space enduring large volume variations during cycles.<sup>17</sup> One-dimensional (1D) and quasi-1D hierarchical MoS<sub>2</sub> nanostructures with a high

<sup>a</sup>State Key Laboratory for Modification of Chemical Fibers and Polymer Materials, College of Materials Science and Engineering, Donghua University, Shanghai 201620, P. R. China. E-mail: czhang@dhu.edu.cn, txliu@dhu.edu.cn, txliu@fudan.edu.cn

<sup>b</sup>Key Laboratory of Flexible Electronics (KLOFE) & Institute of Advanced Materials (IAM), Jiangsu National Synergetic Innovation Center for Advanced Materials (SICAM), Nanjing Tech University (Nanjing Tech), 30 South Puzi Road, Nanjing 211816, P. R. China

<sup>c</sup>School of Chemistry, Physics and Mechanical Engineering, Queensland University of Technology, Brisbane, QLD 4001, Australia

† Electronic supplementary information (ESI) available: SEM images of MoO<sub>3</sub>, SEM and TEM images of MoO<sub>3</sub>@PPy prepared at different pyrrole/MoO<sub>3</sub> ratios. XRD patterns of MoO<sub>3</sub>, MoO<sub>3</sub>@PPy and PPy. SEM images of MoS<sub>2</sub>@NSC after grinding. The XPS survey spectrum and elemental composition of MoS<sub>2</sub>@NSC. SEM and TEM images of MoS<sub>2</sub>@NSC-1 and MoS<sub>2</sub>@NSC-3. XRD patterns of MoO<sub>3</sub>@PPy prepared at different sulfidation temperatures. SEM images of MoS<sub>2</sub>, PPy and NSC. TEM images of NSC. Raman spectra of MoS<sub>2</sub>, MoS<sub>2</sub>@NSC and NSC. XRD patterns of NSC, MoS<sub>2</sub>@NSC, and MoS<sub>2</sub>. TGA curves of MoS<sub>2</sub>, NSC, MoO<sub>3</sub>, and MoS<sub>2</sub>@NSC. CV curves of the MoS<sub>2</sub> electrode. Nyquist plots of MoS<sub>2</sub> and MoS<sub>2</sub>@NSC. TEM images of MoS<sub>2</sub>@NSC and MoS<sub>2</sub> electrodes after 300 cycles. Electrochemical performances of MoS<sub>2</sub>@NSC-1, MoS<sub>2</sub>@NSC-3 and NSC electrodes. Elemental analysis of NSC and MoS<sub>2</sub>@NSC. Performance comparison of MoS<sub>2</sub>-based materials for lithium storage. See DOI: 10.1039/c8nr00068a

aspect ratio are highly attractive due to their largely enhanced electron transport compared with those of MoS<sub>2</sub> in a spherical and polyhedral morphology. In another aspect, the integration of MoS<sub>2</sub> with carbon materials would not only relax the electrode strains during cycles, but also improve the electrical conductivity of the electrodes.<sup>18–20</sup>

Although the construction of hierarchical MoS<sub>2</sub> structures such as spheres and nanowires has been intensely studied, it is still a great challenge to design hierarchical MoS<sub>2</sub> in a rectangular prism shape closely hybridized with carbon materials, which not only renders an effective spacer confinement of MoS<sub>2</sub> during cycles, but also ensures an enhanced electrically conductive pathway. Solvothermal reactions are commonly involved in the preparation of MoS<sub>2</sub>-based materials.<sup>21–24</sup> However, the solvent-free sulfidation strategy provides a versatile and green approach to rapidly produce large quantities of MoS<sub>2</sub> nanosheets, in contrast to the MoS<sub>2</sub> prepared using conventional strategies that require complicated operation such as the use of high-pressure solvothermal conditions, toxic solvents/sulfur sources, or a long reaction time. Therefore, it is still a challenge to explore a low-cost yet effective method to obtain uniform MoS<sub>2</sub>-based composites with enhanced electrochemical performances.

In this work, we develop a solvent-free high-temperature sulfidation strategy to encapsulate hierarchical MoS<sub>2</sub> nanosheets into heteroelement-doped hollow carbon nanoprisms using MoO<sub>3</sub>@polypyrrole (MoO<sub>3</sub>@PPy) core-shell nanoprisms as precursors and sulfur powder as the sulfur source. The solvent-free sulfidation strategy provides a simple and environmentally friendly approach to produce large-scale and high-quality MoS<sub>2</sub> in one batch. Rationally designed hollow polypyrrole nanoprisms were proved to show excellent superiority as unique nanoreactors especially for high-temperature reactions due to the controllable shell thickness and the essence of easy carbonization while maintaining structural stability, which would greatly expand the potential applications of such nanoreactors for high-temperature reactions. Remarkably, the resulting sheet-in-prism superstructures show largely enhanced lithium storage performances in terms of high specific capacity, good rate performance and excellent cycling stability.

## 2. Experimental

### 2.1. Materials

Sodium molybdate dihydrate (Na<sub>2</sub>MoO<sub>4</sub>·2H<sub>2</sub>O, AR), sodium chloride (NaCl, AR), sublimed sulfur (CP), hydrochloric acid (HCl, 37%), ethanol, ammonium persulfate (APS, AR), and *N*-methyl pyrrolidone (NMP) were purchased from Sinopharm Chemical Regent. Pyrrole (AR grade) was obtained from Sigma-Aldrich and distilled before use. Polyvinylidene fluoride (PVDF, Kynar HSV900) was purchased from Arkema Inc. Deionized water (DI water) was used throughout the experiments. All the chemicals were used as received without further purification unless otherwise specified.

### 2.2. Synthesis of the MoO<sub>3</sub> nanoprisms

Typically, Na<sub>2</sub>MoO<sub>4</sub>·2H<sub>2</sub>O (1.21 g) and NaCl (0.60 g) were mixed in 60 mL of DI water, and the pH was adjusted to 1.0 with 3 M HCl. The solution was then transferred to a 100 mL Teflon-lined stainless steel autoclave and kept at 180 °C for 24 h. The products were centrifuged twice for 10 minutes at 5000 rpm, washed successively with 80 mL DI water and 80 mL ethanol in turn three times, and then dried at 60 °C in a vacuum.

### 2.3. Synthesis of MoO<sub>3</sub>@PPy

MoO<sub>3</sub>@PPy composites were prepared by *in situ* oxidative polymerization of pyrrole on MoO<sub>3</sub> using APS as an oxidizer. First, 40 mg of MoO<sub>3</sub> were suspended in 80 mL of DI water, and then designed amounts of pyrrole were added into the suspension and stirred at 0 ± 2 °C for 30 min. Second, 20 mL of APS solution was added dropwise to the above suspension, and the molar ratio of pyrrole and APS was 2/1. The reaction mixture was stirred for 12 h at 0 ± 2 °C, and the precipitates were filtered, washed with 80 mL DI water and 80 mL ethanol in turn three times, and then dried in a vacuum at 60 °C for 12 h. A series of samples were prepared with different initial amounts of pyrrole (*i.e.*, 100, 200 and 400 μL), respectively. For comparison, we synthesized neat PPy through the above-mentioned process without adding MoO<sub>3</sub>.

### 2.4. Synthesis of MoS<sub>2</sub>@nitrogen, sulfur dual-doped carbon (MoS<sub>2</sub>@NSC)

MoO<sub>3</sub>@PPy was ground with sulfur powder in a mortar. The mass ratio of MoO<sub>3</sub>@PPy and sulfur was kept at 1/5. The mixed powder was transferred to a quartz boat, and then heated at 800 °C for 2 h under a N<sub>2</sub> atmosphere at a heating rate of 5 °C min<sup>-1</sup>. The product was dispersed in HCl and stirred for 2 h. After stirring, the product was centrifuged twice at 5000 rpm for 10 min and washed several times with 80 mL DI water, 1 M HCl and acetone to remove any impurities. MoS<sub>2</sub>@NSC-1, MoS<sub>2</sub>@NSC-2 and MoS<sub>2</sub>@NSC-3 were used to represent the MoO<sub>3</sub>@PPy samples prepared with the mass ratio of pyrrole/MoO<sub>3</sub> of 1/10, 2/10 and 4/10, respectively. For comparison, MoS<sub>2</sub> and NSC were prepared by the above-mentioned method using the starting materials MoO<sub>3</sub> and PPy, respectively, instead of MoO<sub>3</sub>@PPy.

### 2.5. Material characterization

The morphologies of the powder products were studied by field-emission scanning electron microscopy (FESEM, JEOL JSM-7001F) and transmission electron microscopy (TEM, JEOL JEM-2100). The crystalline phases of the obtained products were characterized using an X-ray diffractometer on a Bruker D8 Advance. Raman measurements were performed using a Renishaw inVia with a laser wavelength of 633 nm. XPS analysis was conducted on a Karatos Axis ULTRA X-ray photoelectron spectrometer. TGA was performed on a TG 209 F1 from room temperature to 800 °C in air at a heating rate of

10 °C min<sup>-1</sup>. Elemental analysis was conducted using a Vario EL III Element analyzer.

## 2.6. Electrochemical characterization

To prepare the working electrode, the powder sample, carbon black and PVDF binder were mixed in NMP with a weight ratio of 8:1:1. The slurry was pasted onto copper foil with a 1 mg cm<sup>-2</sup> areal loading, and then dried in a vacuum at 80 °C overnight. 2032-type coin cells were assembled using a Celgard 2300 membrane as the separator. The electrolyte was 1 M LiPF<sub>6</sub> dissolved in a mixture of ethyl carbonate and dimethyl carbonate with a volume ratio of 1/1. The cell was assembled in an argon-filled glove box with the concentrations of moisture and oxygen below 1.0 ppm. Galvanostatic discharge-charge tests were performed on a Neware Battery Measurement System (Neware, China) in the voltage range of 0.01–3.0 V. Cyclic voltammetry (CV) measurements were conducted on a CHI 660D electrochemical workstation between 0.01–3.0 V at a scan rate of 0.1 mV s<sup>-1</sup>. Nyquist plots were recorded on the CHI 660D electrochemical workstation at a frequency between 100 kHz and 0.01 Hz.

## 3. Results and discussion

Herein, yolk-shelled MoS<sub>2</sub>@NSC nanoprisms are rationally designed and synthesized, as demonstrated in Fig. 1a. First, PPy shells with a controllable thickness were grown on a MoO<sub>3</sub> nanoprism template, yielding MoO<sub>3</sub>@PPy composites. Second, MoO<sub>3</sub>@PPy mixed with sulfur powder was then pyrolyzed at 800 °C under a N<sub>2</sub> atmosphere, during which the MoO<sub>3</sub> nanoprism core converted into a hierarchical assembly of MoS<sub>2</sub> nanosheets within the PPy shell, and meanwhile the PPy shell nanoreactor could easily convert into NSC hollow nanoprisms which would efficiently prevent the collapse of

hierarchical MoS<sub>2</sub> structures. During pyrolysis, impurities such as excess sulfur were easily removed using a N<sub>2</sub> flow at high temperature. In the above procedure, the thickness of the resulting NSC can be easily controlled by tailoring the thickness of the surrounding PPy shells during *in situ* polymerization of pyrrole. For comparison, bare MoO<sub>3</sub> and *in situ* grown PPy particles were also pyrolyzed by similar sulfidation procedures, yielding the products neat MoS<sub>2</sub> and NSC, respectively. The present approach thus provides a solvent-free sulfidation method for the production of yolk-shelled MoS<sub>2</sub> nanosheets in a hollow carbon nanoprism with a nitrogen/sulfur elemental doping, which are expected to show an enhanced structural stability upon Li<sup>+</sup> insertion after long cycles attributed to an efficient confinement of volume changes of inner MoS<sub>2</sub> nanosheets (Fig. 1b). The as-prepared MoS<sub>2</sub>@NSC is precisely tailored into a yolk-shelled structure of MoS<sub>2</sub> nanosheets in a NSC hollow nanoprism, where the NSC can enhance the electrical conductivity and structural stability of MoS<sub>2</sub>, while the internal MoS<sub>2</sub> may afford largely exposed active sites and abundant micro-/mesopores as ion reservoirs (Fig. 1c).<sup>25</sup>

Morphologies of the MoO<sub>3</sub> templates, the intermediates MoO<sub>3</sub>@PPy and the final products MoS<sub>2</sub>@NSC were characterized and are shown in Fig. 2. The MoO<sub>3</sub> template with a smooth surface shows a uniform nanoprism morphology with a width and length of 150–200 nm and 3–8 μm, respectively (Fig. 2a and S1, ESI†). A high-resolution transmission electron microscopy (HRTEM) image of MoO<sub>3</sub> indicates a crystalline distance of 0.37 nm for the (100) lattice plane of α-MoO<sub>3</sub> (Fig. 2d). Upon the growth of PPy, MoO<sub>3</sub>@PPy (pyrrole/MoO<sub>3</sub> = 10/2 in mass) shows a uniform PPy shell with an average thickness of ~50 nm on the surface of MoO<sub>3</sub> (Fig. 2b and e). We investigated the effect of the PPy concentrations during *in situ* polymerization on the final morphologies of PPy shells while keeping other conditions unaltered. Fig. S2a and S2b (ESI†)

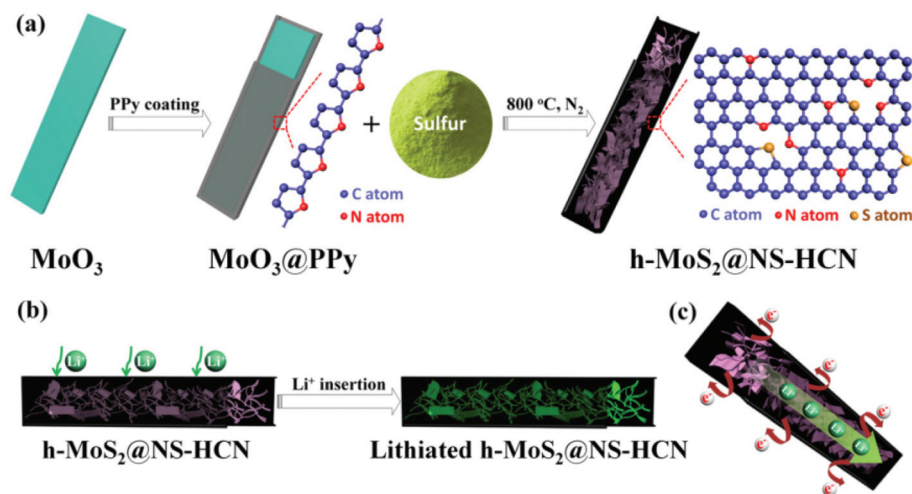


**Fig. 1** (a) Schematic illustration of the formation of yolk-shelled MoS<sub>2</sub>@nitrogen, sulfur dual-doped carbon (MoS<sub>2</sub>@NSC) nanoprisms. (b) Schematic illustration of the Li<sup>+</sup> insertion/extraction process of MoS<sub>2</sub>@NSC nanoprisms. (c) Schematic representation of MoS<sub>2</sub>@NSC nanoprisms with fascinating fast electron and ion transport.

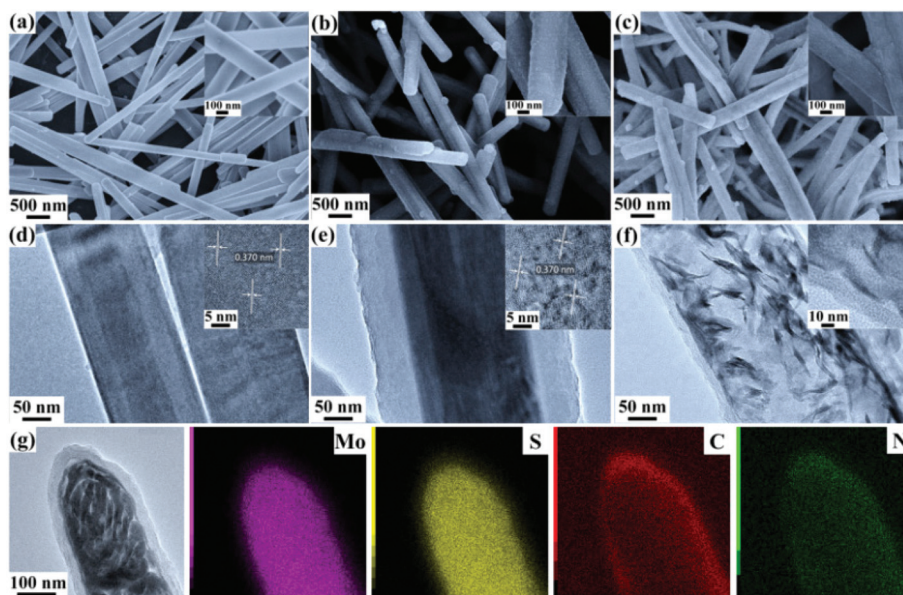


**Fig. 2** SEM and TEM images of (a, d)  $\text{MoO}_3$  nanoprisms, (b, e)  $\text{MoO}_3$ @PPy, and (c, f)  $\text{MoS}_2$ @NSC nanoprisms. The inset of (d) shows a HRTEM image of  $\text{MoO}_3$  nanobelts. The inset of (a–c) shows a high-magnification SEM image of  $\text{MoO}_3$ ,  $\text{MoO}_3$ @PPy and  $\text{MoS}_2$ @NSC nanoprisms. The inset of (d, e) shows a HRTEM image of the (100) lattice planes of  $\alpha$ - $\text{MoO}_3$  within  $\text{MoO}_3$  and  $\text{MoO}_3$ @PPy. The inset of (f) shows a HRTEM image of  $\text{MoS}_2$  nanoflakes within  $\text{MoS}_2$ @NSC nanoprisms. (g) Bright-field TEM image of the  $\text{MoS}_2$ @NSC nanoprisms with corresponding EDS elemental mappings of Mo, S, C and N.

show the field emission scanning electron microscopy (FESEM) and TEM images of  $\text{MoO}_3$ @PPy with a thinner PPy shell of  $\sim 40$  nm, when the mass ratio of pyrrole/ $\text{MoO}_3$  was kept at 10/4. Excess PPy would aggregate into spheres attached on the outer surface of PPy shells when further increasing the mass ratio of pyrrole/ $\text{MoO}_3$  to 10/1 (Fig. S2c and S2d, ESI<sup>†</sup>). X-ray diffraction (XRD) analyses further illustrate the successful compositions of  $\text{MoO}_3$  with PPy during the *in situ* polymerization (Fig. S3, ESI<sup>†</sup>). After the simultaneous pyrolysis and sulfidation process, the overall nanoprism morphology of  $\text{MoS}_2$ @NSC (Fig. 2c) is well preserved with a width of 300–500 nm, which shrinks slightly compared with the intermediate  $\text{MoO}_3$ @PPy. The nanoprism shape of  $\text{MoS}_2$ @NSC-2 is shown in Fig. S4 (ESI<sup>†</sup>). During high-temperature pyrolysis, the PPy shell converts into NSC hollow nanoprisms and the shell thickness of the NSC was estimated to be  $\sim 20$  nm (Fig. 2f), and the solid  $\text{MoO}_3$  nanobelt core converts into hierarchically assembled  $\text{MoS}_2$  nanosheets. The HRTEM image (inset in Fig. 2f) indicates a crystalline distance of 0.625 nm corresponding to the  $\text{MoS}_2$  (002) lattice plane, suggesting the successful conversion from  $\text{MoO}_3$  to 2H-phase  $\text{MoS}_2$ . The TEM image and the corresponding elemental mappings of Mo, S, C and N in  $\text{MoS}_2$ @NSC are shown in Fig. 2g. The element C is mainly distributed in hollow carbon walls, while Mo shows a uniform distribution in the  $\text{MoS}_2$  core, indicating the successful conversion of  $\text{MoO}_3$  into  $\text{MoS}_2$  and the carbonization of PPy into carbon materials during the pyrolysis. Specifically, the two elements N and S distribute along the outline of hollow carbon walls, clearly indicating that N and S are successfully doped into the carbon shells. Moreover, the XPS results (Fig. S5, ESI<sup>†</sup>) also corroborated well with these EDS

mapping results. Accurate contents of C, N and S elements within NSC and  $\text{MoS}_2$ @NSC-2 are shown in Table S1,† based on a combustion elemental analysis method. All three  $\text{MoO}_3$ @PPy samples with diverse morphologies of PPy shells successfully converted into  $\text{MoS}_2$ @NSC (Fig. S6, ESI<sup>†</sup>). Note that  $\text{MoS}_2$ @NSC-1,  $\text{MoS}_2$ @NSC-2 and  $\text{MoS}_2$ @NSC-3 were used to represent the  $\text{MoO}_3$ @PPy samples prepared with the mass ratio of pyrrole/ $\text{MoO}_3$  of 1/10, 2/10 and 4/10, respectively. Unless specially noted,  $\text{MoS}_2$ @NSC was used to denote  $\text{MoS}_2$ @NSC-2 for clarity in the following.

The structural evolution from  $\text{MoO}_3$ @PPy to  $\text{MoS}_2$ @NSC was monitored with TEM characterization (Fig. 3). The vapor pressures of  $\text{MoO}_3$  and sulfur play a critical role during sulfidation, and their vapor pressures are profoundly affected by different temperatures.<sup>26</sup> Therefore, the intermediate products were collected at different reaction stages where the sulfidation temperature was set at 400, 600 and 800 °C, respectively. XRD analysis was conducted to further schematically illustrate the exact compositional evolution during the sulfidation. When the sulfidation temperature reaches 400 °C, the solid  $\text{MoO}_3$  nanoprism begins to break into nanoflakes (Fig. 3a and b). The XRD pattern (Fig. S7, ESI<sup>†</sup>) indicates that the product is a mixture of  $\alpha$ - $\text{MoO}_3$  (JCPDS no. 35-0609) and  $\text{MoO}_2$  (JCPDS no. 032-0671) without the signals of  $\text{MoS}_2$ . At this stage, significant sulfur vapor is generated, which partially reduces  $\text{MoO}_3$  into  $\text{MoO}_2$  nanoflakes. Note that the melting point of  $\text{MoO}_2$  is significantly higher than that of  $\text{MoO}_3$ ; once  $\text{MoO}_3$  was reduced to  $\text{MoO}_2$ , the evaporation of Mo sources would be drastically reduced, and a further sulfidation reaction would proceed within the PPy nanoreactor. When the sulfidation temperature reaches 600 °C, nanosheets of lateral sizes of

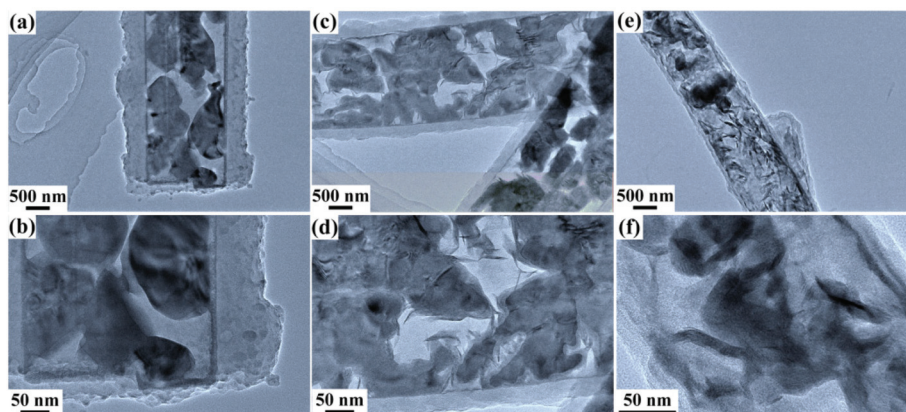


Fig. 3 TEM images of the MoO<sub>3</sub>@PPy sample after the sulfidation treatment at (a, b) 400 °C, (c, d) 600 °C, and (e, f) 800 °C, respectively.

50–100 nm form around the edges of each individual nanoflake (Fig. 3c and d). Meanwhile, the outer PPy shell becomes thinner than that of MoO<sub>3</sub>@PPy treated at 400 °C. For the XRD patterns of MoO<sub>3</sub>@PPy at 600 °C, the characteristic patterns of α-MoO<sub>3</sub> become weaker, accompanied by the appearance of some characteristic patterns ascribed to the formation of 2H-MoS<sub>2</sub> (JCPDS no. 37-1492).<sup>27</sup> The conversion process from MoO<sub>3</sub> to MoS<sub>2</sub> nanosheets by sulfurization involves not only a substitution process from oxygen to sulfur within the MoO<sub>3</sub>, but also migration and redistribution of Mo atoms. Therefore, voids can be observed when forming discrete MoS<sub>2</sub> nanosheets from solid MoO<sub>3</sub> precursors with an orthorhombic structure from the crystal symmetry.<sup>26,28</sup> From the surface energy viewpoint, the MoO<sub>3</sub> nanobelts are favorable to grow along the (001) direction,<sup>29</sup> while 2H-MoS<sub>2</sub> belongs to hexagonal crystals. MoS<sub>2</sub> typically shows highly anisotropic layered structures with trigonal prisms, where each S–Mo–S layer is linked by weak van der Waals interaction.<sup>30</sup> Two general kinds of surface sites exist on these crystals: terrace sites on the basal planes and edge sites on the side surfaces. Due to the anisotropic bonding and the general tendency to minimize the surface energy, nanoparticles of layer materials usually exhibit a sheet morphology with greatly exposed basal planes.<sup>31,32</sup> When further increasing the sulfidation temperature to 800 °C, the XRD patterns indicate that MoO<sub>3</sub> totally converts into 2H-MoS<sub>2</sub>, and no signals of impurities such as α-MoO<sub>3</sub> and MoO<sub>2</sub> are detected. What is more, the thickness of the outer carbon shell becomes thinner when increasing the sulfidation temperature, revealing the simultaneous carbonization of the PPy shell during sulfidation. Hence, individual conversion processes can be included when MoO<sub>3</sub>@PPy reacts with sulfur at a certain temperature. One is the sulfidation of the MoO<sub>3</sub> core into MoS<sub>2</sub>, and this process may be initially promoted by the sulfur source supply, since sulfur can partially reduce MoO<sub>3</sub> to MoO<sub>2</sub> and MoS<sub>2</sub>, involving the sulfur substitutions, lattice reorganizations and redistributions of Mo-based materials. The other is the carbonization and sulfur doping of the PPy shell into NSC hollow nanoprisms. The outer NSC contributes to the stabilization of the overall yolk-shelled nanoprism morphology of the

composites. For comparative analysis, bare MoO<sub>3</sub> nanoprisms are used as precursors in the same sulfidation process, and the resulting MoS<sub>2</sub> exhibits a hierarchical structure assembled by MoS<sub>2</sub> nanosheets with a lateral size of 100–200 nm (Fig. S8, ESI†). Neat PPy particles are also prepared and sulfidized into NSC. Neat PPy exhibits a sponge-like structure with interconnected PPy particles of ~200 nm sizes (Fig. S9, ESI†). After sulfidation, the NSC products maintain the sponge-like structure similar to that of neat PPy with highly vesiculated particles (Fig. S10, ESI†).

XRD and X-ray photoelectron spectroscopy (XPS) were further carried out to analyze the composition of the products. Fig. 4a shows the XRD patterns of MoS<sub>2</sub> and MoS<sub>2</sub>@NSC. The diffraction patterns can be indexed to hexagonal MoS<sub>2</sub> in both samples (JCPDS no. 37-1492), confirming that MoO<sub>3</sub> successfully converts into MoS<sub>2</sub>. The single broad diffraction peak at  $2\theta = \sim 25^\circ$  is observed in MoS<sub>2</sub>@NSC, corresponding to the (002) diffraction of graphitic micro-crystallites (also confirmed

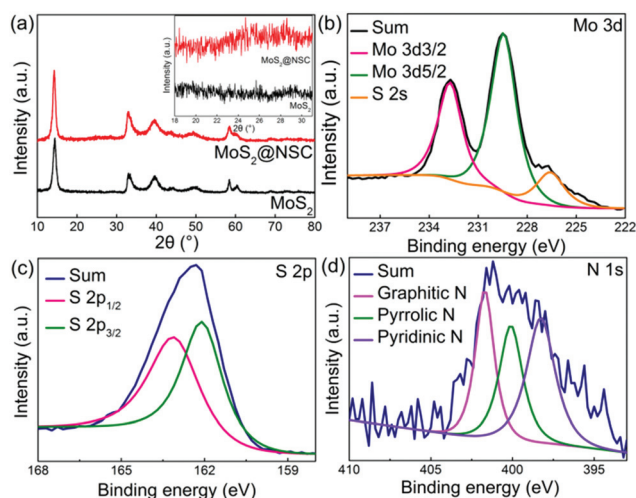
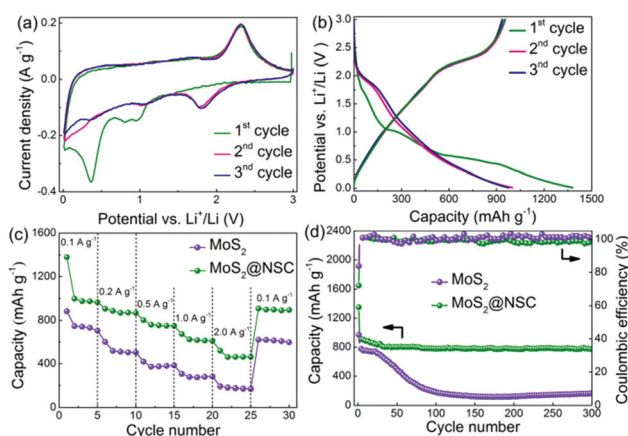


Fig. 4 (a) XRD patterns of MoS<sub>2</sub> and MoS<sub>2</sub>@NSC nanoprisms. The inset of (a) is the enlarged area of 18°–27°. XPS spectra of MoS<sub>2</sub>@NSC nanoprisms: (b) Mo 3d, (c) S 2p, and (d) N 1s.

by Raman spectra in Fig. S11, ESI†). XRD characterization of MoS<sub>2</sub>@NSC prepared from MoO<sub>3</sub>@PPy precursors with different PPy shell thicknesses also indicates the successful sulfidation of MoO<sub>3</sub> into 2H-phase MoS<sub>2</sub> by the simultaneous pyrolysis and sulfidation process (Fig. S12, ESI†). XPS was utilized to determine the oxidation states of Mo, S and N in MoS<sub>2</sub>@NSC. In Fig. 4b, the intense Mo 3d<sub>5/2</sub> and Mo 3d<sub>3/2</sub> components located at 229.5 and 232.7 eV are characteristic of MoS<sub>2</sub>.<sup>33</sup> In Fig. 4c, S 2p XPS spectra show a strong peak at 162.5 eV, which was ascribed to S<sup>2-</sup>. Fitting the N 1s signals (Fig. 4d) indicates the presence of three different types of nitrogen species, pyridinic N (398.2 eV), pyrrolic N (400.1 eV), and graphitic N (401.7 eV), in good agreement with other N-doped carbon materials.<sup>34</sup> As expected, the large proportion of pyridinic and graphitic nitrogen within MoS<sub>2</sub>@NSC would be beneficial for improving the electrochemical performance of such electrode materials in LIBs.<sup>34,35</sup> In addition, TGA analysis (Fig. S13, ESI†) was performed in air to estimate the composition of MoS<sub>2</sub>@NSC. Assuming that MoS<sub>2</sub> completely convert to MoO<sub>3</sub> and NSC are oxidized to CO<sub>2</sub>, the mass fraction of MoS<sub>2</sub> within MoS<sub>2</sub>@NSC-1, MoS<sub>2</sub>@NSC-2 and MoS<sub>2</sub>@NSC-3 can be determined to be ~94.6%, 90.7% and 83.6%, respectively.

To highlight the superiority of MoS<sub>2</sub>@NSC as an anode material for LIBs, we performed an electrochemical evaluation of MoS<sub>2</sub>@NSC and MoS<sub>2</sub>. The cyclic voltammogram (CV) curves of the first, second and third cycle were obtained to understand the mechanism of these electrode materials during the electrochemical evolution, as shown in Fig. 5a. There are three cathodic peaks located at 0.95, 0.80 and 0.36 V in the first cycle, which correspond to the intercalations of Li ions into MoS<sub>2</sub> interlayers to form Li<sub>x</sub>MoS<sub>2</sub>, the additional insertion of Li ions into the expanded space and edge sites of MoS<sub>2</sub>, and the irreversible conversion reaction of Li<sub>x</sub>MoS<sub>2</sub> into Li<sub>2</sub>S and Mo metal.<sup>36</sup> The slope below 0.3 V is ascribed to the formation of a solid electrolyte interphase (SEI) film. The

distinct peak located at 2.32 V is associated with the delithiation of Li<sub>2</sub>S. During the following cathodic/anodic scans, peaks overlap well demonstrating good reversibility for the intercalation and de-intercalation of Li ions. In the third cycle, cathodic peaks centered at 1.82, 1.03 and 0.39 V, which can be attributed to the conversion from S<sub>8</sub> to Li<sub>2</sub>S, the formation of Li<sub>x</sub>MoS<sub>2</sub> and the conversion reaction process, respectively.<sup>36</sup> For MoS<sub>2</sub>, the CV profiles (Fig. S14, ESI†) are similar to those of MoS<sub>2</sub>@NSC, indicating that the surrounded NSC does not change the electrochemical reaction in the electrode. The representative galvanostatic discharge/charge voltage profiles of MoS<sub>2</sub>@NSC at a current density of 0.1 A g<sup>-1</sup> in a voltage window of 0.01–3 V are shown in Fig. 5b. There are two voltage plateaus at ~1.1 and 0.6 V in the first discharge process, owing to the access of Li ions to the MoS<sub>2</sub> interlayer and the conversion of MoS<sub>2</sub> into Mo particles, respectively.<sup>37</sup> The voltage plateau at ~2.3 V in the first charge cycle is attributed to the delithiation of Li<sub>2</sub>S.<sup>37</sup> The MoS<sub>2</sub>@NSC electrode delivers an initial discharge and charge capacity of 1400 and 1000 mA h g<sup>-1</sup>, respectively, providing an initial Coulombic efficiency (CE) as high as 72%. The irreversible capacity loss is mainly attributed to the inevitable formation of SEI films. Meanwhile, the CE of the MoS<sub>2</sub>@NSC electrode in the second and third cycles reaches as high as 97% and 98%, respectively. Fig. 5c shows the rate capability of the MoS<sub>2</sub>@NSC electrode by cycling at various current densities ranging from 0.1 to 2 A g<sup>-1</sup>. The MoS<sub>2</sub>@NSC electrode delivers average specific capacities of 960, 850, 720, 610, and 440 mA h g<sup>-1</sup> at current densities of 0.1, 0.2, 0.5, 1, and 2 A g<sup>-1</sup>, respectively. Table S2† summarizes and compares the lithium storage performances of the MoS<sub>2</sub>@NSC nanoprisms with other MoS<sub>2</sub>-based composites. Considering the simple and green approach for the construction of the MoS<sub>2</sub>@NSC nanoprisms using the solvent-free sulfidation method, the electrochemical performances of our study are comparable to most reported MoS<sub>2</sub>-based composites using solvothermal and CVD approaches. Remarkably, a stable capacity at ~900 mA h g<sup>-1</sup> of the MoS<sub>2</sub>@NSC electrode was recovered when further reducing the current density back to 0.1 A g<sup>-1</sup>, implying a high capacity reversibility. For comparison, the rate capacity performances of the MoS<sub>2</sub> electrode were also evaluated. The neat MoS<sub>2</sub> electrode shows a much lower capacity of 720, 500, 400, 300, and 180 mA h g<sup>-1</sup>, respectively, at current densities from 0.1 to 2 A g<sup>-1</sup>, respectively, and only a recovery capacity of 580 mA h g<sup>-1</sup> was obtained when the current density returns to 0.1 A g<sup>-1</sup> with limited rate capacity because of its poor transportation of electrons and ions. The superior ion-diffusion kinetics performances of the MoS<sub>2</sub>@NSC electrode are also revealed by electrochemical impedance spectroscopy (EIS) analysis (Fig. S15, ESI†). The two semicircles are observed in the Nyquist plot of neat MoS<sub>2</sub>. The intercept of the first semicircle in the high frequency region represents the ohmic series resistance (R<sub>s</sub>) related to the intrinsic resistance of the assembled cells.<sup>38</sup> The first semicircle corresponds to the resistance of the SEI film, whereas the medium frequency semicircle is associated with the charge transfer resistance of the electrode/electrolyte interface, and



**Fig. 5** Electrochemical characterization of the MoS<sub>2</sub>@NSC electrode for LIBs: (a) CV curves at a scan rate of 0.2 mV s<sup>-1</sup>, (b) discharge-charge voltage profiles at a current density of 0.1 A g<sup>-1</sup>, (c) rate capability, and (d) cycling performance at a current density of 0.1 A g<sup>-1</sup>.

the inclined line is related to the Warburg impedance caused by the diffusion of Li ions within the electrodes. Compared with the neat MoS<sub>2</sub> electrode, the MoS<sub>2</sub>@NSC-2 electrode shows a much smaller diameter of semicircles in the high-frequency region, indicating a lower charge-transfer resistance ( $R_{ct}$ ) at the electrode/electrolyte interface due to the conductive outer NSC.<sup>39</sup> Moreover, a more vertical straight line is observed for the MoS<sub>2</sub>@NSC electrode in the low-frequency region, implying better ion diffusion within the electrode matrix.

The MoS<sub>2</sub>@NSC electrode exhibits excellent capacity retention at 0.1 A g<sup>-1</sup> (Fig. 5d). The capacity remains as high as 800 mA h g<sup>-1</sup> after 300 cycles, far beyond the reversible capacity delivered by the MoS<sub>2</sub> electrode (103 mA h g<sup>-1</sup> after 300 cycles). The microstructure of the MoS<sub>2</sub>@NSC electrode after 300 cycles was investigated by TEM observation (Fig. S16, ESI†). The integrity of such a yolk-shelled structure was generally preserved after cycling, which further confirms that the outstanding electrochemical properties were derived from well encapsulation of the NSC protective layers. The effect of the diverse morphologies of NSC on the electrochemical performance of the MoS<sub>2</sub>@NSC electrode was also investigated and discussed in the ESI (Fig. S17 and S18†), and moreover, the electrochemical performance of the NSC electrode was measured to validate the important role of the MoS<sub>2</sub> core in the final electrochemical performance of the composites (see detailed discussion in Fig. S19, ESI†). The excellent electrochemical performance of MoS<sub>2</sub>@NSC might be attributed to the increased number of electrochemically active sites compared with the closely stacked MoS<sub>2</sub> solid.<sup>40</sup> The hierarchical MoS<sub>2</sub>@NSC exhibits fascinating properties as a potential anode material for LIBs benefitting from their unique structural characteristics like a well-defined hollow interior to relieve the structural strain during cycles and ultrathin 2D microcells to expose more efficient electrochemically active sites.

## 4. Conclusions

In summary, we report a simultaneous pyrolysis and sulfidation process for the topochemical formation of hierarchical MoS<sub>2</sub> in nitrogen, sulfur dual-doped carbon (MoS<sub>2</sub>@NSC) yolk-shelled nanoprisms. By using MoO<sub>3</sub>@PPy as the precursor and sulfur powder as the sulfur source, the solid-vapor reaction between MoO<sub>3</sub> solid and sulfur vapor takes place at elevated temperatures within the unique PPy nanoreactor, which is easily chemically doped and carbonized maintaining its structural stability even at 800 °C under nitrogen. Benefiting from the structural and compositional features, the as-obtained MoS<sub>2</sub>@NSC nanoprisms deliver an excellent lithium-storage performance including a high specific capacity (960 mA h g<sup>-1</sup> at 0.1 A g<sup>-1</sup>), excellent rate performance (440 mA h g<sup>-1</sup> at 2 A g<sup>-1</sup>) and good cycling stability (maintaining as high as 800 mA h g<sup>-1</sup> after 300 cycles) that enable their potential applications in next-generation energy storage devices.

## Conflicts of interest

There are no conflicts to declare.

## Acknowledgements

We are grateful for the financial support from the National Natural Science Foundation of China (51773035, 51433001 and 21504012), the Fundamental Research Funds for the Central Universities (17D110606), the Program of Shanghai Subject Chief Scientist (17XD1400100) and the Natural Science Foundation of Shanghai (17ZR1439900).

## References

- 1 M. Armand and J. M. Tarascon, *Nature*, 2008, **451**, 652–657.
- 2 B. Dunn, H. Kamath and J. M. Tarascon, *Science*, 2011, **334**, 928–935.
- 3 W. Yin, J. Yu, F. Lv, L. Yan, L. R. Zheng, Z. Gu and Y. Zhao, *ACS Nano*, 2016, **10**, 11000–11011.
- 4 D. Kong, J. Luo, Y. Wang, W. Ren, T. Yu, Y. Luo, Y. Yang and C. Cheng, *Adv. Funct. Mater.*, 2014, **24**, 3815–3826.
- 5 K. Zhao, L. Zhang, R. Xia, Y. Dong, W. Xu, C. Niu, L. He, M. Yan, L. Qu and L. Mai, *Small*, 2016, **12**, 588–594.
- 6 J. S. Chen, L. A. Archer and X. W. Lou, *J. Mater. Chem.*, 2011, **21**, 9912–9924.
- 7 X. W. Lou, D. Deng, J. Y. Lee, J. Feng and L. A. Archer, *Adv. Mater.*, 2008, **20**, 258–262.
- 8 G. Zhang, H. B. Wu, T. Song, U. Paik and X. W. D. Lou, *Angew. Chem., Int. Ed.*, 2014, **53**, 12590–12593.
- 9 X. Geng, W. Sun, W. Wu, B. Chen, A. Al-Hilo, M. Benamara, H. Zhu, F. Watanabe, J. Cui and T.-p. Chen, *Nat. Commun.*, 2016, **7**, 10672.
- 10 Y. Sun, S. Gao, F. Lei and Y. Xie, *Chem. Soc. Rev.*, 2015, **44**, 623–636.
- 11 Q. Liu, Q. Fang, W. Chu, Y. Wan, X. Li, W. Xu, M. Habib, S. Tao, Y. Zhou, D. Liu, T. Xiang, A. Khalil, X. Wu, M. Chhowalla, P. M. Ajayan and L. Song, *Chem. Mater.*, 2017, **29**, 4738–4744.
- 12 N. Savjani, E. A. Lewis, M. A. Bissett, J. R. Brent, R. A. W. Dryfe, S. J. Haigh and P. O'Brien, *Chem. Mater.*, 2016, **28**, 657–664.
- 13 A. B. Laursen, S. Kegnaes, S. Dahl and I. Chorkendorff, *Energy Environ. Sci.*, 2012, **5**, 5577–5591.
- 14 C. Pham, J. H. Choi, J. Yun, A. S. Bandarenka, J. Kim, P. V. Braun, S. Y. Jeong and C. R. Cho, *ACS Nano*, 2017, **11**, 1026–1033.
- 15 A. Jawaid, D. Nepal, K. Park, M. Jespersen, A. Qualley, P. Mirau, L. F. Drummy and R. A. Vaia, *Chem. Mater.*, 2015, **28**, 337–348.
- 16 K. Leng, Z. Chen, X. Zhao, W. Tang, B. Tian, C. T. Nai, W. Zhou and K. P. Loh, *ACS Nano*, 2016, **10**, 9208–9215.
- 17 L. Zhou, Z. C. Zhuang, H. H. Zhao, M. T. Lin, D. Y. Zhao and L. Q. Mai, *Adv. Mater.*, 2017, **29**, 1602914.

- 18 H. Jiang, D. Ren, H. Wang, Y. Hu, S. Guo, H. Yuan, P. Hu, L. Zhang and C. Li, *Adv. Mater.*, 2015, **27**, 3687–3695.
- 19 S. J. Ding, J. S. Chen and X. W. Lou, *Chem. – Eur. J.*, 2011, **17**, 13142–13145.
- 20 K. Chang, D. S. Geng, X. F. Li, J. L. Yang, Y. J. Tang, M. Cai, R. Y. Li and X. L. Sun, *Adv. Energy Mater.*, 2013, **3**, 839–844.
- 21 L. C. Yang, S. N. Wang, J. J. Mao, J. W. Deng, Q. S. Gao, Y. Tang and O. G. Schmidt, *Adv. Mater.*, 2013, **25**, 1180–1184.
- 22 F. Sun, Y. Wei, J. Chen, D. Long, L. Ling, Y. Li and J. Shi, *Nanoscale*, 2015, **7**, 13043–13050.
- 23 X. Hu, Y. Li, G. Zeng, J. Jia, H. Zhan and Z. Wen, *ACS Nano*, 2018, **12**, 1592–1602.
- 24 J.-G. Wang, R. Zhou, D. Jin, K. Xie and B. Wei, *Electrochim. Acta*, 2017, **231**, 396–402.
- 25 C. Zhang, H. B. Wu, Z. Guo and X. W. Lou, *Electrochem. Commun.*, 2012, **20**, 7–10.
- 26 P. Taheri, J. Q. Wang, H. Xing, J. F. Destino, M. M. Arik, C. Zhao, K. F. Kang, B. Blizzard, L. J. Zhang, P. Q. Zhao, S. M. Huang, S. Yang, F. V. Bright, J. Cerne and H. Zeng, *Mater. Res. Express*, 2016, **3**, 075009.
- 27 L. Najafi, S. Bellani, B. Martín-García, R. Oropesa-Nuñez, A. E. Del Rio Castillo, M. Prato, I. Moreels and F. Bonaccorso, *Chem. Mater.*, 2017, **29**, 5782–5786.
- 28 S. Hong, A. Krishnamoorthy, P. Rajak, S. Tiwari, M. Misawa, F. Shimojo, R. K. Kalia, A. Nakano and P. Vashishta, *Nano Lett.*, 2017, **17**, 4866–4872.
- 29 X.-L. Li, J.-F. Liu and Y.-D. Li, *Appl. Phys. Lett.*, 2002, **81**, 4832–4834.
- 30 R. R. Chianelli, E. B. Prestridge, T. A. Pecoraro and J. P. Deneufville, *Science*, 1979, **203**, 1105–1107.
- 31 T. F. Jaramillo, K. P. Jorgensen, J. Bonde, J. H. Nielsen, S. Horch and I. Chorkendorff, *Science*, 2007, **317**, 100–102.
- 32 J. Xie, H. Zhang, S. Li, R. Wang, X. Sun, M. Zhou, J. Zhou, X. W. Lou and Y. Xie, *Adv. Mater.*, 2013, **25**, 5807–5813.
- 33 J. Kibsgaard, Z. Chen, B. N. Reinecke and T. F. Jaramillo, *Nat. Mater.*, 2012, **11**, 963–969.
- 34 A. L. M. Reddy, A. Srivastava, S. R. Gowda, H. Gullapalli, M. Dubey and P. M. Ajayan, *ACS Nano*, 2010, **4**, 6337–6342.
- 35 Y. Mao, H. Duan, B. Xu, L. Zhang, Y. Hu, C. Zhao, Z. Wang, L. Chen and Y. Yang, *Energy Environ. Sci.*, 2012, **5**, 7950–7955.
- 36 K. Chang and W. X. Chen, *ACS Nano*, 2011, **5**, 4720–4728.
- 37 F. Zhou, S. Xin, H. W. Liang, L. T. Song and S. H. Yu, *Angew. Chem., Int. Ed.*, 2014, **53**, 11552–11556.
- 38 M. Tebyetekerwa, X. Wang, Y. Wu, S. Yang, M. Zhu and S. Ramakrishna, *J. Mater. Chem. A*, 2017, **5**, 21114–21121.
- 39 J.-M. Jeong, K. G. Lee, S.-J. Chang, J. W. Kim, Y.-K. Han, S. J. Lee and B. G. Choi, *Nanoscale*, 2015, **7**, 324–329.
- 40 J. Li, Y. Hou, X. Gao, D. Guan, Y. Xie, J. Chen and C. Yuan, *Nano Energy*, 2015, **16**, 10–18.